

CARBON-ENHANCED METAL-POOR STARS: CEMP-S AND CEMP-NO SUB-CLASSES IN THE HALO SYSTEM OF THE MILKY WAY

DANIELA CAROLLO¹Dept. of Physics and Astronomy - Astronomy, Astrophysics and Astrophotonic Research Center
Macquarie University - North Ryde, 2109, NSW, Australia

KEN FREEMAN

Research School of Astronomy & Astrophysics, Australian National University
& Mount Stromlo Observatory, Cotter Road, Weston, ACT, 2611, Australia

TIMOTHY C. BEERS

National Optical Astronomy Observatory, Tucson, AZ, 85719, USA
and JINA: Joint Institute for Nuclear Astrophysics

VINICIUS M. PLACCO

Gemini Observatory, Hilo, HI 96720, USA

JASON TUMLINSON

Space Telescope Science Institute, Baltimore, MD, 21218, USA

SARAH L. MARTELL

Australian Astronomical Observatory, North Ryde, 2109, NSW, Australia

ABSTRACT

We explore the kinematics and orbital properties of a sample of 323 very metal-poor stars in the halo system of the Milky Way, selected from the high-resolution spectroscopic follow-up studies of Aoki et al. and Yong et al. The combined sample contains a significant fraction of carbon-enhanced metal-poor (CEMP) stars (22% or 29% , depending on whether a strict or relaxed criterion is applied for this definition). Barium abundances (or upper limits) are available for the great majority of the CEMP stars, allowing for their separation into the CEMP-*s* and CEMP-no sub-classes. A new method to assign membership to the inner- and outer-halo populations of the Milky Way is developed, making use of the integrals of motion, and applied to determine the relative fractions of CEMP stars in these two sub-classes for each halo component. Although limited by small-number statistics, the data suggest that the inner halo of the Milky Way exhibits a somewhat higher relative number of CEMP-*s* stars than CEMP-no stars (57% vs. 43%), while the outer halo possesses a clearly higher fraction of CEMP-no stars than CEMP-*s* stars (70% vs. 30%). Although larger samples of CEMP stars with known Ba abundances are required, this result suggests that the dominant progenitors of CEMP stars in the two halo components were different; massive stars for the outer halo, and intermediate-mass stars in the case of the inner halo.

Subject headings: Galaxy: Evolution, Galaxy: Formation, Galaxy: Halo, Galaxy: Structure, Stars: Abundances, Carbon, Surveys

1. INTRODUCTION

The halo system of the Milky Way hosts the vast majority of the presently observed metal-poor (MP: $[\text{Fe}/\text{H}] < -1.0$) and very metal-poor (VMP; $[\text{Fe}/\text{H}] < -2.0$) stars. These objects are of special interest, as they preserve a fossil record of the nucleosynthesis products of the first generations of stars that formed shortly after the Big Bang, and hence offer a unique opportunity to explore the early stages of galaxy formation

and the chemical evolution of galactic halos.

1.1. *The Halo System of the Milky Way*

Although once thought of as a comparatively simple component, the halo system of the Milky Way is apparently complex. It comprises at least two main structural components, the diffuse inner- and the outer-halo populations, numerous detected sub-structures, such as streams and overdensities (Grillmair 2009, and references therein), as well as a substantial number of globular clusters. Recently, ages determined from white dwarf cooling sequences, and other methods, have indicated differences (of up to 2 Gyrs) in the ages of clusters and field stars that can be associated with the inner- and outer-halo populations (Kalirai 2012; Hansen et al. 2013a).

The dual nature of the diffuse halo was initially recognized

daniela.carollo@mq.edu.au
kcf@mso.anu.edu.au
beers@noao.edu
vplacco@gemini.edu
tumlinson@stsci.edu
smartell@aao.gov.au

¹ INAF-Osservatorio Astronomico di Torino, Pino Torinese, Italy

by Carollo et al. (2007, 2010, hereafter C07 and C10), based on analyses of the kinematics of a local sample of calibration stars from the Sloan Digital Sky Survey (SDSS; York et al. 2000; Gunn et al. 2006). These authors demonstrated that the inner and outer halos possess different peak metallicities (inner: $[\text{Fe}/\text{H}] \sim -1.6$; outer: $[\text{Fe}/\text{H}] \sim -2.2$), as well as different spatial distributions, with the inner halo exhibiting a flatter density profile than the nearly spherical outer halo. According to their analysis, the inner-halo component is essentially non-rotating, while the outer-halo component exhibits a significant retrograde signature. The velocity ellipsoids of the populations also differ, in the sense that the outer-halo population is clearly “hotter” than the inner-halo population.

The proposed duality of the Galactic halo has been confirmed by other authors, based on different data sets. For example, de Jong et al. (2010) analysed stellar number-density maps constructed from the “vertical” photometric stripes obtained during the SEGUE-1 sub-survey of SDSS (Yanny et al. 2009), and identified a shift in the peak stellar metallicity as a function of Galactocentric distance ($[\text{Fe}/\text{H}] \sim -1.6$ at $r < 15$ kpc ; $[\text{Fe}/\text{H}] \sim -2.2$ at $r > 15$ -20 kpc), similar to the shift in the peak of the MDF argued to be present by C07 and C10, and occurring at the same halo transition radius, r_{HTR} ,² as inferred from their kinematical analysis. Kinman et al. (2012) identified signatures of the retrograde nature of the outer-halo population from samples of RR Lyrae stars chosen without kinematic bias, reporting that the transition from a flattened, essentially non-rotating inner halo to a spherical, retrograde outer halo occurs beyond about 12.5 kpc. Similar evidence for retrograde motions have been described in Hattori et al. (2013) and Kafle et al. (2013), based on samples of blue horizontal-branch (BHB) stars with available metallicities and radial velocities from SDSS. Additional lines of evidence supporting the dual halo of the Milky Way have been reported by Beers et al. (2012). Most recently, An et al. (2013) have used photometric estimates of stellar metallicity for stars in SDSS Stripe 82 to argue that, even in the relatively nearby volume (5-8 kpc from the Sun), the observed metallicity distribution function (MDF), coupled with the kinematics of the local halo, is incompatible with a single population of stars.

The bimodality of the MDF in the halo system of M 31 is now also well-established. Sarajedini et al (2012) report evidence of a bimodal MDF in the halo of M31 with peaks at $[\text{Fe}/\text{H}] \sim -1.3$ and $[\text{Fe}/\text{H}] \sim -1.9$. Ibata et al. (2013) found that the metallicity of the smooth halo of M 31 decreases from $[\text{Fe}/\text{H}] \sim -0.9$ at $r = 27$ kpc, down to $[\text{Fe}/\text{H}] \sim -1.9$ at $r = 150$ kpc. A similar metallicity shift is reported by Gilbert et al. (2013) and Gilbert et al. (in preparation), who identify a clear change in the peak in the MDF of M 31’s diffuse halo population at around $r_{\text{HTR}} \sim 40$ kpc, from a peak of $[\text{Fe}/\text{H}] \sim -0.4$ inside this radius to $[\text{Fe}/\text{H}] \sim -1.5$ outside this radius. Numerical simulations of hierarchical galaxy formation (in particular those including baryons; Tissera et al. 2013b, and references therein) produce dual-halo systems that share many of the observed properties of the Milky Way and M 31. For discussion of a contrary view, see, e.g., Schönrich et al. (2011) and Beers et al. (2012).

² The halo transition radius is defined by Tissera et al. (2013b) to denote the region in their simulated galaxies marking the transition from relative dominance by the stellar inner-halo population to the stellar outer-halo population.

1.2. Carbon-Enhanced Metal-Poor Stars in the Halo System of the Milky Way

The distribution of carbon on iron ($[\text{C}/\text{Fe}]$) for halo stars provides a clear indication of differences in the chemical nature of the inner- and outer-halo populations. Carbon-enhanced metal-poor (CEMP) stars have been defined as a subset of MP and VMP stars that exhibit elevated $[\text{C}/\text{Fe}]$ ($[\text{C}/\text{Fe}] \geq +1.0$; Beers & Christlieb 2005). Other authors have used slightly different criteria, e.g., $[\text{C}/\text{Fe}] \geq +0.7$ (Aoki et al. 2007; Carollo et al. 2012; Norris et al. 2013b). In the past two decades, it has been recognized that ~ 15 -20% of stars with $[\text{Fe}/\text{H}] < -2.0$ are carbon enhanced (Beers et al. 1992; Norris et al. 1997; Rossi et al. 1999; Beers & Christlieb 2005; Cohen et al. 2005; Marsteller et al. 2005; Rossi et al. 2005; Frebel et al. 2006; Lucatello et al. 2006; Norris et al. 2007; Carollo et al. 2012; Cohen et al. 2013; Norris et al. 2013b; Spite et al. 2013). This fraction rises to 30% for $[\text{Fe}/\text{H}] < -3.0$, to 40% for $[\text{Fe}/\text{H}] < -3.5$, and $\sim 75\%$ for $[\text{Fe}/\text{H}] < -4.0$ (with the inclusion an apparently carbon-normal star with $[\text{Fe}/\text{H}] = -4.9$ by Caffau et al. 2011). This increasing trend of CEMP-star frequency with declining $[\text{Fe}/\text{H}]$ is again confirmed from the many thousands of CEMP stars found among the several hundred thousand stars with available medium-resolution spectra from SDSS, SEGUE-1, and SEGUE-2 (Rockosi et al., in preparation), as described by Lee et al. (2013). It is presumably no coincidence that the most extreme iron-deficient star known, the septa metal-poor ($[\text{Fe}/\text{H}] < -7.0$) star SMSS J031300.36-670839.3, exhibits both carbon enhancement and the characteristic light-element enhancement associated with the CEMP-no class (Keller et al. 2014).

Carollo et al. (2012) estimated $[\text{C}/\text{Fe}]$ for the sample of over 30,000 SDSS/SEGUE calibration stars used by C10. In addition to the rise in the cumulative frequency of CEMP stars at lower metallicity, they also confirmed a significant increase in the level of carbon enrichment in CEMP stars, as a function of decreasing metallicity, growing from $\langle [\text{C}/\text{Fe}] \rangle \sim +1.0$ at $[\text{Fe}/\text{H}] = -1.5$ to $\langle [\text{C}/\text{Fe}] \rangle \sim +1.7$ at $[\text{Fe}/\text{H}] = -2.7$. In the same paper it was shown that the carbon-on-iron distribution function (CarDF) changes dramatically with increasing distance from the Galactic plane. For $|Z| < 5$ kpc, relatively few CEMP stars are identified (over all metallicities). For distances $|Z| > 5$ kpc, the CarDF exhibits a strong tail towards higher values, up to $[\text{C}/\text{Fe}] > +3.0$. Carollo et al. (2012) sought to establish whether these effects are related to metallicity, or to changes in the nature of the stellar population with distance above the plane. In the metallicity interval $-2.5 < [\text{Fe}/\text{H}] \leq -2.0$, there is evidence for a significant contrast in the frequency of CEMP stars that are kinematically assigned to the inner- and outer-halo components, such that $F_{\text{CEMP}_{\text{out}}} \sim 2 \times F_{\text{CEMP}_{\text{in}}}$. The increase in the frequency of CEMP stars with distance from the Galactic plane can then be understood in the context of the greater fraction of outer-halo population stars that are found farther from the plane.

In any case, the large fraction of CEMP stars at low metallicity indicates that significant amounts of carbon were produced in the early stages of chemical evolution in the universe. The observed contrast of the CEMP-star fractions in the inner- and outer-halo populations strengthens the picture that these halo components had different origins. Carollo et al. (2012) speculated that this could be understood if the progenitors of stars in the outer-halo population included additional early-universe sources of carbon production, an idea we explore

further in the present paper.

1.2.1. CEMP Sub-Classes

Beers & Christlieb (2005) specify a nomenclature that identifies a number of sub-classes for CEMP stars. The CEMP-*s* stars exhibit over-abundances of elements produced by the so-called slow neutron-capture process, or *s*-process, such as barium. These stars are the most commonly observed subclass of CEMP stars; around 80% of CEMP stars exhibit *s*-process-element enhancements (Aoki et al. 2007), including both the CEMP-*s* and CEMP-*r/s* sub-classes (the latter subclass indicates stars for which the presence of both *r*- and *s*-process element enhancements are found). The favored scenario for the production of CEMP-*s* (CEMP-*r/s*) stars is mass transfer of carbon- and *s*-process-enhanced material from the envelope of an asymptotic giant-branch (AGB) star to its (presently observed) binary companion (e.g., Herwig 2005; Sneden et al. 2008). Observational evidence now exists to suggest that the CEMP-*r/s* stars (and other *r*-process-element rich stars) were enhanced in *r*-process elements in their natal gas clouds by previous generations of supernovae (SNe), and did not require a contribution of *r*-process elements from a binary companion (see Hansen et al. 2011, 2013b).

By contrast, the CEMP-no stars exhibit no strong neutron-capture-element enhancements, and are preferentially found at lower metallicity than the CEMP-*s* and CEMP-*r/s* stars (Aoki et al. 2007). Possible progenitors for CEMP-no stars include massive, rapidly rotating, mega metal-poor (MMP; $[\text{Fe}/\text{H}] < -6.0$) stars, which models suggest have greatly enhanced abundances of CNO due to distinctive internal burning and mixing episodes, followed by strong mass loss (Hirschi et al. 2006; Meynet et al. 2006, 2010). Another proposed mechanism is pollution of the interstellar medium by so-called faint supernovae associated with the first generations of stars, which experience extensive mixing and fallback during their explosions (Umeda & Nomoto 2003, 2005; Tominaga et al. 2007, 2013; Ito et al. 2009, 2013; Kobayashi et al. 2011; Nomoto et al. 2013).

Extant radial-velocity data support the expected differences in the binary nature of CEMP-*s* (CEMP-*r/s*) and CEMP-no stars. Lucatello et al. (2005) argued that multiple-epoch radial-velocity measurements of CEMP-*s* stars are consistent with essentially all CEMP-*s* (CEMP-*r/s*) stars being members of binary systems. Although more data is desired for CEMP-no stars, Hansen et al. (2013b) report that the fraction of binaries among stars within this sub-class is no higher than expected for random samples of VMP giants. Cohen et al. (2013) and Norris et al. (2013b) reach similar conclusions, based on their limited radial-velocity data for CEMP-no stars.

In this paper we make use of the CEMP sub-classes to explore the chemical differences between the inner- and outer-halo components of the Galaxy. We employ a combined sample of over 300 VMP and extremely metal-poor (EMP; $[\text{Fe}/\text{H}] < -3.0$) stars recently investigated by Aoki et al. (2013), Norris et al. (2013a), Norris et al. (2013b), and Yong et al. (2013).

Stars in this sample have available high-quality, high-resolution spectroscopy, sufficient to enable the classification of the CEMP stars they contain into the CEMP-*s* or CEMP-no sub-classes (we do not attempt to resolve the CEMP-*r/s* from the CEMP-*s* sub-class in this paper). We use their reported radial velocities, distances, and (where available) proper motions in order to derive full space motions for these stars. Then, through use of an energy and angular momentum cri-

terion to assign each CEMP star to either the inner-halo or outer-halo population, we evaluate the relative numbers of CEMP-*s* and CEMP-no stars that are likely to be associated with each halo component.

The paper is organized as follows. Section 2 summarizes our combined stellar sample, and describes the radial velocities, distance estimates, assembly of proper motions, and assignment of the CEMP sub-classes. In Section 3, the space motions and orbital properties of the stars in our combined sample are derived, together with the integrals of motion. This section also describes our methods for assignment of the stars' membership into the inner- or outer-halo populations, and reports the relative numbers of CEMP-*s* and CEMP-no stars for the two halo components. Finally, Section 4 considers the implications of these results for the formation and evolution of the Galactic halo populations.

2. DESCRIPTION OF THE COMBINED SAMPLE

Our dataset is assembled from the samples of stars discussed in Aoki et al. (2013), and in the series of papers by Norris et al. (2013a), Norris et al. (2013b), and Yong et al. (2013). For convenience, we simply refer to the first source as the Aoki et al. sample, and the latter three sources as the Yong et al. sample. These studies are based on high-resolution follow-up observations of VMP and EMP targets identified in the massive SDSS-I and SDSS-II/SEGUE moderate-resolution spectroscopic data sets, the Hamburg/ESO (HES) objective-prism survey (Wisotzki et al. 1996; Christlieb et al. 2001; Christlieb 2003; Christlieb et al. 2008), the HK survey (Beers et al. 1985, 1992), and on additional data compiled from the literature. Elemental abundances have been adopted from Cohen et al. (2013) for three stars in the Yong et al. sample, and from Roederer et al. (2014) for two stars in the Yong et al. sample; these were adopted when either the Yong et al. sample reported no C or Ba abundance, or only had an upper limit for one or both of these elements available. Although clear selection biases for the inclusion of very metal-poor stars exist in the Aoki et al. and Yong et al. samples (by design), stars with or without carbon enhancement were not specifically targeted by either group. As with most all high-dispersion spectroscopic follow-up studies, preference was given in the selection of targets to include brighter stars (although in the case of the Aoki et al. sample, this is curtailed by the bright limit of $g \sim 14.5$ among SDSS stars). However, as emphasized by the An et al. (2013) analysis of an *unbiased* sample of stars (with respect to metallicity), the fraction of outer-halo stars *even in the local neighborhood* is roughly similar to the fraction of inner-halo stars at low metallicity (see their Figure 18). Hence, we expect that at least a representative sample of objects drawn from both populations can be achieved in the metallicity range explored by the combined sample.

The Aoki et al. sample comprises 137 stars, 28 of which have reported C determinations, and 42 of which have Ba abundances reported. These stars were observed at high spectral resolution ($R \sim 30000$), in the course of four observing runs between March and October 2008, using the High Dispersion Spectrograph (Noguchi et al. 2002) at the Subaru Telescope. This sample includes a large number of warmer main-sequence turnoff stars, which (at the signal-to-noise obtained for the majority of the sample, $S/N \sim 20 - 30$) present a challenge to obtain these abundance measurements. We also include 190 stars from the Yong et al. sample – the 38 stars from their “program sample”, and 152 stars in their litera-

ture compilation. This sample comprises 171 stars with C measurements or upper limits, and 175 stars with Ba abundances or upper limits. High-resolution spectra ($22000 < R < 85000$) of the program sample stars were taken between June 2007 and September 2008, using the MIKE spectrograph (Bernstein et al. 2003) on the Magellan Clay Telescope at Las Campanas Observatory, the HIRES spectrograph (Vogt et al. 1994) at Keck Observatory, or the UVES spectrograph (Dekker et al. 2000) on VLT UT2 (Kueyen) at the European Southern Observatory. The selection of the program stars and the literature compilation is explained in Yong et al. (2013), and the determination of stellar parameters is described by Norris et al. (2013a) and Yong et al. (2013). In the case of the Yong et al. literature sample, the authors adopt the measured equivalent widths from the literature, and performed their own analysis to determine stellar parameters and abundances. Tables 1 and 2 list the observed properties of the Aoki et al. and Yong et al. samples, respectively.

There are four stars in common between the Aoki et al. sample and the Yong et al. sample, indicated with superscript “f” next to the star name in column (1) of Table 1 and “j” in Table 2. For the purpose of the analysis described below, we adopt the parameters from the Yong et al., as they were able to obtain estimates or upper limits on [C/Fe] and [Ba/Fe] for these four stars, while Aoki et al. (2013) (using lower S/N spectra) reported no measurements of these abundance ratios. There are thus 323 unique stars in our combined sample. This sample is pared further, as described below, to only include stars for which kinematical parameters could be estimated.

2.1. Radial Velocities

Radial velocities for the stars in the Aoki et al. sample are taken from their high-resolution spectroscopic determinations, which have errors typically less than 1 km s^{-1} . Our adopted radial velocities are listed in column (5) of Table 1, with the associated errors given in column (6).

Radial velocities for the stars from the Yong et al. sample are taken from their high-resolution spectroscopic determinations, which have errors typically less than 1 km s^{-1} , although some have errors as large as 3 km s^{-1} . Our adopted radial velocities and errors for this sample are listed in columns (5) and (6) of Table 2, respectively.

2.2. Distance Estimates

Distances for the stars in the Aoki et al. sample were assigned making use of their surface gravity estimates in order to classify stars as dwarfs, main-sequence turnoff stars, or giants, then using the V magnitudes and adopted $E(B-V)$ reddening provided by Aoki et al. (2013) to apply the procedures described by Beers et al. (2012), and references therein. These procedures are based on a set of absolute magnitude relationships (using absorption and reddening-corrected Johnson V magnitudes and $B-V$ colors) calibrated to Galactic globular and open clusters, as described by Beers et al. (2000; their Table 2). As demonstrated in Beers et al. (2000), photometric distances estimated for their sample are in good agreement with distances derived from accurate Hipparcos parallaxes. We have taken care to apply the revised procedure described by Beers et al. (2012) in carrying out the luminosity-class assignments prior to assigning distances. The resulting distances should be accurate to on the order of 10%-20%, based on previous tests. Our adopted distances are listed in column (13) of Table 1.

Norris et al. (2013b) derived distances for their stars via a straightforward spectroscopic parallax method – using the final stellar parameters from Yong et al. (2013), they find the absolute magnitude M_V predicted by the Y^2 isochrones for each star, then use the available apparent V magnitudes and $E(B-V)$ reddening values to calculate distances. Note that Norris et al. (2013b) only published distances for stars in their sample with $[\text{FeH}] \leq -3.1$; J. Norris (private communication) kindly applied this approach for the remaining stars in the Yong et al. sample for our use. Our adopted distances for these stars, which are expected to have similar accuracy as the distances for the Aoki et al. (2013) sample, $\sim 15\%$, are listed in column (13) of Table 2.

There are two stars in the Yong et al. sample for which well-measured distance estimates are not available. These stars, indicated with an “a” superscript next to the star name in column (1) in Table 2, are dropped from further consideration in the kinematic analysis that follows.

2.3. Proper Motions

Proper motions for the Aoki et al. stars were taken from the SDSS stellar database, if the measurement satisfied the criteria of Munn et al. (2004), designed to eliminate spurious reported motions. Note that all proper motions have been corrected for the systematic error described by Munn et al. (2008). The adopted proper motions are listed in columns (9) and (10) of Table 1. The typical errors for individual proper-motion components (listed in columns (11) and (12) of Table 1) are on the order of $\sim 2\text{-}3 \text{ mas yr}^{-1}$.

There are two stars in the Aoki et al. sample for which well-measured proper motions are not available. These stars, indicated with a “b” superscript next to the star name in column (1) in Table 1, are dropped from further consideration in the kinematic analysis that follows.

Proper motions for the Yong et al. stars have been obtained by matching the sample stars with the UCAC-4 (Zacharias et al. 2013), SPM-4 (Girard et al. 2011), or PPMXL (Roeser et al. 2010) catalogs. Our adopted proper motions are listed in columns (9) and (10) of Table 2. The typical errors for individual proper-motion components (listed in columns (11) and (12) of Table 2) are on the order of $\sim 2\text{-}4 \text{ mas yr}^{-1}$, although a number of stars have substantially higher proper-motion errors.

2.4. CEMP Classifications

Carbon on iron, [C/Fe], and barium on iron, [Ba/Fe], abundance ratios are reported for the Aoki et al. and Yong et al. samples in columns (14) and (15) of Tables 1 and 2, respectively. We have assigned a set of codes to each star in the combined sample, given in columns (16) and (17) of Tables 1 and 2, to indicate the availability and status of a C and Ba measurement for that star. In column (16), C = 0 indicates the absence of a C measurement; C = 1 indicates that the carbon status for that star is indeterminate (an upper limit on [C/Fe] $> +0.7$); C = 2 indicates that the star is considered C-normal ([C/Fe] $< +0.7$); C = 3 indicates that the star is considered a CEMP star ([C/Fe] $\geq +0.7$). In column (17), Ba = 0 indicates the lack of a Ba measurement; Ba = 1 indicates that the Ba status for that star is indeterminate (an upper limit on [Ba/Fe] > 0.0); Ba = 2 indicates that the star is considered Ba-normal ($0.0 < [\text{Ba/Fe}] < +1.0$); Ba = 3 indicates that the star is considered Ba-enhanced ($[\text{Ba/Fe}] \geq +1.0$); Ba = 4 indicates that the star is considered Ba-deficient ($[\text{Ba/Fe}] \leq 0.0$).

Note that many of the stars in the combined sample lack Eu measurements, which precludes use of the [Ba/Eu] abundance ratio necessary to discriminate between the CEMP-*s* and CEMP-*r/s* sub-classes, according to the taxonomy of Beers & Christlieb (2005). However, as noted above, our current understanding of the progenitors of the CEMP-*r/s* sub-class necessarily involves the same mass-transfer episodes as for the CEMP-*s* stars, presumably onto a star that had formed from an ISM that had already been enhanced in *r*-process elements. Note that no Eu abundance measurement is required in order to assign the CEMP-no sub-class.

For the purpose of our following analysis, we classify the CEMP stars with [Ba/Fe] $\geq +1.0$ as CEMP-*s* (which could include some CEMP-*r/s* stars); those with [Ba/Fe] ≤ 0.0 are considered CEMP-no stars. Column (18) of Tables 1 and 2 list the assigned sub-classifications for the CEMP stars in the Aoki et al. and Yong et al. samples, respectively. There are a total of 70 stars in the combined sample which are classified as CEMP, of which 40 are assigned to be CEMP-*s*, 24 are assigned to be CEMP-no, and 6 are not sub-classifiable, due to a missing Ba measurement. We refer to these stars as our ‘‘Strict Sample’’ (hereafter, SS), indicating that the stars passed all tests needed to clearly assign their status. There are two additional stars that we add to the SS, the canonical CEMP-no stars HE 0107-5240 (Christlieb et al. 2002) and HE 1327-2326 (Frebel et al. 2005), both of which are formally considered Ba-indeterminate, due to their high upper limits on [Ba/Fe], but that clearly belong to this sub-class on the basis of their light-element abundance patterns. The 6 stars that were not sub-classifiable, but which meet the strict criterion for inclusion as CEMP stars, we label ‘‘CSS,’’ indicating that they are carbon-enhanced stars.

Because we are battling low-number statistics, we have also considered another sub-sample of stars, which we refer to as the ‘‘Extended Sample’’ (ES). This sample includes all of the SS (and CSS) stars, as well as (1) stars that are within reasonable error bars (as summarized in the table notes) of being classified as CEMP, and/or CEMP-*s* and CEMP-no, (2) stars that have light-element abundance patterns that suggest a CEMP-no classification, (3) stars that are expected to be CEMP-no, based on their low metallicity and the detection limit for Ba at their (lower) temperatures in the Aoki et al. sample, or (4) stars that are considered CEMP according to the luminosity criterion of Aoki et al. (2007)³. Such stars are indicated by superscripts ‘‘d’’ or ‘‘e’’ next to the star names in column (1) of Tables 1 and 2.

There are a total of 96 stars in the combined sample that meet the more relaxed criteria described above, of which 42 are assigned to be CEMP-*s*, 46 are assigned to be CEMP-no, and 8 stars that are not further sub-classifiable, due to a missing Ba measurement; these 8 stars we label ‘‘CSS’’ or ‘‘CES,’’ indicating that they are carbon-enhanced stars. By definition, the ES includes all of the stars in the SS, and the CES stars include the CSS stars. Column (19) of Tables 1 and 2 provides a four digit code, where each digit takes on the value 1 or 0, depending on its classification according to this scheme. The digits correspond to the classes SS, ES, CSS, or CES. For example, a code 1100 would indicate that the star is a member of the SS and the ES, but not the CSS or the CES.

The upper panel of Figure 1 shows the distribution of [Fe/H] for all the stars in our combined sample. In the bot-

tom panel the unshaded histogram represents the MDF for the 88 CEMP stars of the SS or ES (as well as the 8 CSS or CES stars, which could not be further sub-classified), the light gray distribution applies to the 42 SS or ES stars assigned to the CEMP-*s* sub-class, and the cross-hatched distribution indicates the MDF for the 46 SS or ES stars assigned to the CEMP-no sub-class. All of the CEMP-no stars are located in the metallicity regime [Fe/H] < -2.5 , in agreement with the metallicity trend first identified by Aoki et al. (2007). The lowest metallicity CEMP-*s* star in our sample has [Fe/H] = -3.5 .

3. KINEMATIC ANALYSIS

3.1. Derivation of Space Motions and Orbital Properties

The combination of radial velocities, distances, and proper motions for our sample stars are used to calculate the full space motions. The velocity components (U, V, W) are relative to the Local Standard of Rest (LSR), where U is taken to be positive in the direction toward the Galactic anticenter, V is positive in the direction of Galactic rotation, and W is positive toward the North Galactic Pole. The velocities are corrected for the motion of the Sun with respect the LSR by adopting the values (U, V, W) = $(-9, 12, 7)$ km s⁻¹ (Mihalas & Binney 1981). We have also evaluated the rotational velocity in the cylindrical Galactocentric reference frame, with its origin at the center of the Galaxy. This velocity is denoted as V_ϕ , and is calculated assuming that the LSR is on a circular orbit with a value of 220 km s⁻¹ (Kerr & Lynden-Bell 1986). In our calculations, we assume a value for the location of the Sun at $R_\odot = 8.5$ kpc. These values are consistent with recent independent determinations of these quantities by Ghez et al. (2008), Koposov et al. (2009), and Bovy et al. (2012).

The orbital parameters of the stars are derived by adopting an analytic Stäckel-type gravitational potential, which consists of a flattened, oblate disk, and a nearly spherical massive dark-matter halo (see the description given by Chiba & Beers 2000, Appendix A). The peri-Galactic distance, r_{peri} , is defined as the closest approach of an orbit to the Galactic center, while the apo-Galactic distance, r_{apo} , is the farthest extent of an orbit from the Galactic center. The orbital eccentricity, e , is defined as $e = (r_{\text{apo}} - r_{\text{peri}})/(r_{\text{apo}} + r_{\text{peri}})$, while Z_{max} is the maximum distance of a stellar orbit above or below the Galactic plane. In addition, we evaluate the integrals of motion for any given orbit, deriving the energy, E , and the angular momentum in the vertical direction, $L_z = R \times V_\phi$. Note that R represents the distance from the Galactic center projected onto the disk plane. Typical errors on the orbital parameters (at $Z_{\text{max}} < 50$ kpc; C10) are: $\sigma_{r_{\text{peri}}} \sim 1$ kpc, $\sigma_{r_{\text{apo}}} \sim 2$ kpc, $\sigma_{\text{ecc}} \sim 0.1$, $\sigma_{Z_{\text{max}}} \sim 1$ kpc.

Based on the derived orbital parameters, there are four stars in the Aoki et al. sample and 14 stars in the Yong et al. sample that are formally unbound from the Galaxy. These stars, indicated with a ‘‘c’’ superscript next to the star name in column (1) of Tables 1 and 2, are dropped from further consideration in the kinematic analysis that follows.

Taking into account all of the stars dropped from the two samples, as described above, we proceed with the kinematic analysis based on 127 stars from the Aoki et al. sample (4 stars that also appear in the Yong et al. sample are dropped) and 174 stars from the Yong et al. sample, for a total of 301 stars. Among the CEMP stars, there are a total of 64 stars suitable for the kinematic analysis in the SS, and 88 in the ES. In order to avoid confusion, we refer to this full set of

³ The Aoki et al. (2007) luminosity criterion is: [C/Fe] $\geq +0.7$, for $\log(L/L_\odot) \leq 2.3$ and (ii) [C/Fe] $\geq +3.0 - \log(L/L_\odot)$, for $\log(L/L_\odot) > 2.3$.

program stars with suitable kinematic determinations as the “Total Kinematic Sample” and the sub-sample of CEMP stars within it as the “CEMP Kinematic Sample.”

3.2. The Energy-Angular Momentum Diagram: Membership Assignment to the Inner- and Outer-Halo Populations

We now seek to evaluate the relative numbers of CEMP-s and CEMP-no stars in the inner- and outer-halo populations contained in the CEMP Kinematic Sample, which requires that a population assignment be made. In Carollo et al. (2012), such a division was accomplished by employing the extreme deconvolution technique (Bovy et al. 2011), applied to the rotational velocity distribution of the low-metallicity sub-sample of the SDSS/SEGUE DR7 calibration stars. This technique is not suitable for the present sample, due to the limited number of stars that are available. We explore a new method below, comparing with a large external sample of stars, before returning to the kinematic analysis of our program stars.

3.2.1. A New Method of Kinematic Population Assignment; Testing the SDSS/SEGUE DR7 Calibration Stars

An alternative method to that previously used employs the integrals of motion, such as the total energy, E , and the angular momentum in the vertical direction, L_Z . To explore this approach, we have calculated the integrals of motion for the SDSS/SEGUE DR7 calibration stars used by C10⁴. The results are shown in Figure 2 as an energy-angular momentum diagram, also known as the Lindblad diagram.

The point sizes in the two panels of Figure 2 are proportional to the logarithmic number density at a given point of the diagram, while the colors denote different ranges of metallicity. According to C10, the thick disk has a mean Galactocentric rotational velocity of $\langle V_\phi \rangle = 182 \text{ km s}^{-1}$, and a velocity dispersion, $\sigma(V_\phi) = 51 \text{ km s}^{-1}$, which correspond to a mean angular momentum of $\langle L_Z \rangle \sim 1550 \text{ kpc km s}^{-1}$, and a range of angular momentum between $L_Z \sim 1100$ and $2000 \text{ kpc km s}^{-1}$ (at the one-sigma level). Thick-disk stars are highly bound to the Galaxy, have a peak in their MDF at $[\text{Fe}/\text{H}] \sim -0.6$, and dominate the light blue area in the Lindblad diagram (upper panel). The metal-weak thick-disk (MWTD) population, when treated as an independent component (as in C10), exhibits a mean Galactocentric rotational velocity $\langle V_\phi \rangle \sim 100\text{--}150 \text{ kpc km s}^{-1}$, and a velocity dispersion of $\sigma_{V_\phi} \sim 40 \text{ km s}^{-1}$. These values correspond to a mean angular momentum of $\langle L_Z \rangle \sim 1000 \text{ kpc km s}^{-1}$, and angular momentum in the range $700\text{--}1300 \text{ kpc km s}^{-1}$ (one-sigma). MWTD stars are highly bound to the Galaxy, exhibit a peak in their MDF at $[\text{Fe}/\text{H}] \sim -1.2$ (C10), and are clearly present in the Lindblad diagram, as represented by red filled dots in the top panel of Figure 2.

C07 and C10 have shown that the inner-halo population is dominated by stars on high-eccentricity orbits, with the majority of inner-halo stars having apo-Galactic distances not greater than $r_{\text{apo}} = 15 \text{ kpc}$, a mean Galactocentric rotational velocity $\langle V_\phi \rangle \sim 0$, with a velocity dispersion of $\sigma_{V_\phi} \sim 100 \text{ km s}^{-1}$ (roughly a Gaussian distribution symmetrical about $L_Z \sim 0$). Based on these values, the location of the majority of the inner-halo population in the Lindblad diagram would

be in the range of $-850 \text{ kpc km s}^{-1} < L_Z < 850 \text{ kpc km s}^{-1}$ (at the one-sigma level), and mostly clustered in a narrow region around $L_Z = 0 \text{ kpc km s}^{-1}$. This is clearly visible in the top panel of Figure 2, where the green area denotes stars with metallicity in the range $-2.0 < [\text{Fe}/\text{H}] \leq -1.3$; this interval was selected to bound the metallicity peak of the inner-halo population ($[\text{Fe}/\text{H}] = -1.6$), and to reduce contamination from MWTD stars.

The inner-halo stars are mostly highly bound (lower energy values), but also comprise stars with higher energy orbits, $E > -1.0 \text{ km}^2 \text{ s}^{-2}$ (in units of 10^5), and are clearly visible in the top panel of Figure 2. The outer-halo population is characterized by a wide range of eccentricity values, with a significant number of outer-halo stars having low to intermediate orbital eccentricities, and the majority having apo-Galactic distances $r_{\text{apo}} > 15 \text{ kpc}$. The mean Galactocentric rotational velocity of the outer-halo stars is $\langle V_\phi \rangle \sim -85 \text{ km s}^{-1}$, with a velocity dispersion of $\sigma_{V_\phi} = 165 \text{ km s}^{-1}$. In the Lindblad diagram, the outer-halo stars are primarily located in the region characterized by retrograde motions, at $L_Z < -700 \text{ kpc km s}^{-1}$, and with high-energy orbits. The metallicity peak of the outer halo is $[\text{Fe}/\text{H}] \sim -2.2$, and includes many of the stars with $[\text{Fe}/\text{H}] < -2.0$, represented in Figure 2 (top panel) by black filled circles.

In the bottom panel of Figure 2, the red dashed curve denotes the locus that would apply for stars possessing orbits with apo-Galactic distance $r_{\text{apo}} = 15 \text{ kpc}$. This is derived using the expression for the energy $E = L_Z^2/2r^2 + \Phi(r, Z)$, and $V_r = 0$, where $\Phi(r, Z)$ is the Galactic potential, and r is in kpc. The locus of the points in the (E, L_Z) plane for $r_{\text{apo}} = 15 \text{ kpc}$ and $Z = 0$ is $E = (L_Z^2)/(2 \times 15^2) + \Phi(15, 0)$. All of the data points located below this curve have orbits with $r_{\text{apo}} < 15 \text{ kpc}$, while those located above the curve have $r_{\text{apo}} > 15 \text{ kpc}$. The inner-halo population is characterized by stars with $r_{\text{apo}} < 15 \text{ kpc}$, and dominates the distribution below this apo-Galactic radius. Stars with metallicity $[\text{Fe}/\text{H}] \leq -1.3$ and apo-Galactic radii $r_{\text{apo}} < 15 \text{ kpc}$ are color-coded green in the figure, while stars in same range of metallicity and apo-Galactic radii $r_{\text{apo}} > 15 \text{ kpc}$ are color-coded blue. Inspection of this part of the diagram reveals that there are a significant number of inner-halo stars with apo-Galactic radii exceeding 15 kpc , however they are mainly clustered below a binding energy of $E = -1.0 \text{ km}^2 \text{ s}^{-2}$ (in units of 10^5 ; represented by the black horizontal line). Above this value of total energy, the stars with $r_{\text{apo}} > 15 \text{ kpc}$ are dominated by retrograde motions.

Another important feature can be noticed from inspection of the bottom panel of Figure 2. The nature of the distribution changes as the energy increases (stars are less bound to the Galaxy), from being roughly a Gaussian distribution centered at $L_Z \sim 0 \text{ kpc km s}^{-1}$ and $E = -1.1 \text{ km}^2 \text{ s}^{-2}$, to becoming increasingly retrograde. The change seems quite abrupt. At the higher energies, the distribution does not appear Gaussian, and for $E > -0.6 \text{ km}^2 \text{ s}^{-2}$, it appears more like a uniform distribution. The more bound Gaussian component could be interpreted as a dynamically relaxed low- L_Z system, which is consistent with a component that formed *in-situ*. The more uniform component could be interpreted as an unrelaxed system made up of accreted material, reflecting the (E, L_Z) distribution at the time that the incoming satellites (the presumed progenitors for many of the outer-halo stars) were disrupted.

The abrupt change of the (E, L_Z) distribution is easily visualized in Figure 3, where the vertical angular momentum

⁴ The distance estimates for the stars in this sample are based on the luminosity-class assignments revised according to the procedures described by Beers et al. (2012).

is plotted against the total energy. The solid line represents a moving average, with overlapping bins of 200 points. In this figure, only the stars with $R_{\text{apo}} > 15$ kpc and $[\text{Fe}/\text{H}] \leq -1.3$ are selected. In this way, we avoid most of the contamination from the MWTD, but are sure to include most of the stars that are members of the inner halo. It is worth noting that, in the region between $E \sim -1.05 \text{ km}^2 \text{ s}^{-2}$ and $-0.9 \text{ km}^2 \text{ s}^{-2}$ (in units of 10^5), there is a clear abrupt change of the mean angular momentum towards retrograde values, going from $\langle L_Z \rangle \sim 0 \text{ kpc km s}^{-1}$ to $\langle L_Z \rangle \sim -600 \text{ kpc km s}^{-1}$ (corresponding to $\langle V_\phi \rangle \sim 0 \text{ km s}^{-1}$ and $\langle V_\phi \rangle \sim -70 \text{ km s}^{-1}$, respectively). The angular momentum becomes more retrograde as the energy increases, achieving a value of $\langle L_Z \rangle \sim -1400 \text{ kpc km s}^{-1}$ (corresponding to $\langle V_\phi \rangle \sim -165 \text{ km s}^{-1}$). Note that $\langle V_\phi \rangle = -70$ is very close to the mean rotational velocity of the outer-halo population ($\langle V_\phi \rangle = -80 \text{ km s}^{-1}$), and $\sigma_{V_\phi} \sim 165 \text{ km s}^{-1}$ corresponds to the velocity dispersion of the outer halo at the one-sigma level. The abrupt change in the L_Z - E diagram shown in Figure 3 can be considered the transition zone between the inner- and outer-halo populations. The mid-point of this zone is $E \sim -0.97 \text{ km}^2 \text{ s}^{-2}$, with an extension up to $-0.9 \text{ km}^2 \text{ s}^{-2}$ on the right end, and $-1.05 \text{ km}^2 \text{ s}^{-2}$ on the left end. Below $E \sim -1.05 \text{ km}^2 \text{ s}^{-2}$, the mean angular momentum averages to $\sim 0 \text{ kpc km s}^{-1}$, while above $E \sim -0.9 \text{ km}^2 \text{ s}^{-2}$, the mean angular momentum is $\sim -1000 \text{ kpc km s}^{-1}$ (corresponding to $\langle V_\phi \rangle \sim -123 \text{ km s}^{-1}$). For the purpose of our analysis, we consider an extended transition zone of $-1.10 < L_Z < -0.82 \text{ km}^2 \text{ s}^{-2}$, in order to take into account the uncertainties.

Based on these properties, among the stars with apo-Galactic distance $R_{\text{apo}} > 15$ kpc and $[\text{Fe}/\text{H}] \leq -1.3$, those with binding energy $E < -1.1 \text{ km}^2 \text{ s}^{-2}$ are likely pure inner-halo stars, while those with binding energy above $E \sim -0.8 \text{ km}^2 \text{ s}^{-2}$ are likely pure outer-halo members. The stars with energy and angular momentum falling in the transition zone of Figure 3 have similar probability of being either inner- or outer-halo stars, according to this criterion. The numbers of stars assigned to the various components from among the 8039 SDSS/SEGUE DR7 calibration stars shown in Figure 3 are: outer halo (274), inner halo (6995), and transition zone (770), respectively. Stars that are on unbound orbits were already dropped from this sample, so are not represented in the figure. For completeness, we note that if the metallicity limit is set to $[\text{Fe}/\text{H}] \leq -2.0$, the numbers of stars assigned to the various components are: outer halo (62), inner halo (1237), and transition zone (159), respectively.

We now return to our program sample, and apply the above approach for the assignment of stars into the inner- and outer-halo populations, based on their energies and integrals of motion.

3.3. Relative Numbers of CEMP-s and CEMP-no Stars in the Inner and Outer halo

The above population assignment procedure is applied to the Total Kinematic Sample of Aoki et al. and Yong et al. Column (20) of Tables 1 and 2 lists the assigned membership for the stars in these samples, respectively. The label ‘‘O’’ indicates outer halo, ‘‘I’’ indicates inner halo, ‘‘T’’ indicates the transition zone, and ‘‘U’’ indicates that the star was unclassified (star is on an unbound orbit, or is missing the information required for making this assignment).

The left-hand panel of Figure 4 shows the Lindblad diagram for the stars in our Total Kinematic Sample (stars in

the U class are obviously not shown). The black filled circles represent C-normal stars, while the red stars denote the CEMP stars (ES and CES). In the right-hand panel of Figure 4, the CEMP-s stars having orbits with $r_{\text{apo}} < 15$ kpc are represented by purple filled triangles, while those with $r_{\text{apo}} > 15$ kpc are denoted by yellow filled diamonds. In the same way, the CEMP-no stars with $r_{\text{apo}} < 15$ kpc are shown as blue asterisks, while those with $r_{\text{apo}} > 15$ kpc are represented by light blue filled squares. The gray dashed curve represents the locus of stars with orbits having $r_{\text{apo}} > 15$ kpc.

The orbital properties found in the previous subsection suggest that stars with apo-Galactic distances below 15 kpc can be considered pure inner-halo members. Stars with apo-Galactic distance greater than 15 kpc and binding energy $E < -1.1 \text{ km}^2 \text{ s}^{-2}$ can be assigned to the inner-halo component as well. Stars with apo-Galactic distance above 15 kpc and binding energy $E > -0.8 \text{ km}^2 \text{ s}^{-2}$ are likely to be pure outer-halo stars. The remaining stars with $r_{\text{apo}} > 15$ kpc and energy between $E \sim -1.1 \text{ km}^2 \text{ s}^{-2}$ and $E \sim -0.8 \text{ km}^2 \text{ s}^{-2}$ fall in the transition zone between the inner-halo population and the outer-halo population, and a clear membership assignment cannot be made.

Table 3 summarizes the population assignments for stars in the Total Kinematic Sample and those in the CEMP Kinematic Sample. Note that for the CEMP stars, the table lists two numbers for each of the membership assignments, the first corresponding to stars in the SS, the second (in parenthesis, and always larger) corresponding to stars in the ES.

For the stars in the CEMP Kinematic Sample assigned to the outer halo, the SS only contains a total of 12 stars, which is too small to obtain a meaningful comparison of the CEMP-s and CEMP-no subclasses. Thus, for our counting exercise, we prefer to make use of the 20 stars in the ES assigned to the outer halo. In this instance, the counts in Table 3 indicate that 70% (14/20) of the stars are CEMP-no, and 30% (6/20) are CEMP-s.

For the stars in the CEMP Kinematic Sample assigned to the inner halo, the 37 stars contained in the SS are sufficient to proceed, and we prefer to use this sub-sample, due to the more secure classifications. In this instance, the counts in Table 3 indicate that 43% (16/37) of the stars are CEMP-no, and 57% are CEMP-s. We caution that, if we were to have compared the proportions of stars in the inner halo based on the ES members, the fraction of CEMP-no stars would be greater (56%) than the CEMP-s stars (44%), underscoring the need for more, and better, classifications of CEMP stars for future tests of our hypothesis.

A one-tailed Z-test of the significance of the change in the proportions of CEMP-no stars in the inner (SS) and outer halo (ES), which automatically takes into consideration of the relative sample sizes, rejects the null hypothesis that the fraction is constant ($p = 0.02$). Even so, this study would clearly benefit from larger samples of confidently classified CEMP-no and CEMP-s stars. For now, we can only tentatively suggest that the CEMP-no stars represent the majority of C-rich stars associated with the outer-halo population, while the CEMP-s stars represent the majority associated with the inner-halo population, at least in this sample of very and extremely low-metallicity CEMP stars.

4. IMPLICATIONS FOR THE FORMATION OF THE HALO SYSTEM

We find that the relative numbers of CEMP-no stars compared to CEMP-*s* stars varies between the inner- and outer-halo components of the Milky Way, with the frequency of CEMP-no stars being higher in the counter-rotating outer halo, and the frequency of CEMP-*s* stars being higher in the non-rotating inner halo. This trend may reflect some underlying difference in the chemical-enrichment histories of the halo components, perhaps due to varying yields in the stellar populations formed by the progenitors of the two components.

The exact origins of the C-enhancement for CEMP stars are not yet fully understood. In the case of the CEMP-*s* stars, mass transfer between binary companions is strongly implied by the abundance patterns and radial-velocity measurements. (Herwig 2005; Sneden et al. 2008; Bisterzo et al. 2011, 2012; Lugaro et al. 2012; Placco et al. 2013). This scenario requires that the binary system form with a low-mass star (the one observed today) and a star in the right mass range to pass through an AGB phase, with significant production of carbon and *s*-process elements, roughly $1.3\text{--}6 M_{\odot}$. Thus, the CEMP-*s* phenomenon is associated with intermediate-mass progenitor stars.

The origin of the C-enhancement for the CEMP-no stars is less clear. One possible scenario involves binary pairings of a low-mass star (the one observed today) and a more massive binary companion that can donate carbon in a mass-transfer event, but which did not produce *s*-process elements (Suda et al. 2007). Another proposed scenario involves “faint SNe”, or core-collapse SNe that exploded with low energy, and undergo a mixing and fallback process, ejecting the C-rich outer layers of the progenitor star but not material from the inner, Fe-rich core regions (Umeda & Nomoto 2003, 2005; Tominaga et al. 2007, 2013; Ito et al. 2009, 2013; Nomoto et al. 2013). In this scenario, CEMP-no stars would arise preferentially from massive progenitors, roughly $10\text{--}60 M_{\odot}$. Hirschi et al. (2006), Meynet et al. (2006), and Meynet et al. (2010) have argued that massive, rapidly rotating, MMP stars, with greatly enhanced abundances of CNO due to distinctive internal burning and mixing episodes, can blow strong winds that can pollute the primordial ISM with this material, with the inner regions possibly collapsing into black holes. Recently, Chiappini (2013) have argued that such sources may be capable of driving an *s*-process, but its nature is at present poorly understood. In any event, the rapidly increasing frequency of CEMP stars with declining [Fe/H] provides clear evidence that sources capable of producing carbon *without* substantial release of iron-peak elements must be common at early times.

If we assume the binary mass-transfer scenario applies for CEMP-*s* stars, and the faint SNe and/or rapidly rotating MMP scenario applies for CEMP-no stars, the implication is that the former dominates in the stellar populations associated with the inner halo, while the latter are more numerous in the populations comprising the outer halo. If the CEMP-*s* and CEMP-no phenomena vary with the mass of the stars that produced the carbon, this requires some variation in the IMF for the progenitor populations of the inner and outer halos. A link between the CEMP phenomenon and the early-universe IMF was suggested previously by Lucatello et al. (2005), Suda et al. (2007), Tumlinson (2007a), and Tumlinson (2007b), among others. The necessary variations can be accommodated with

relatively small changes to the IMF: the ratio of the number of CEMP-no progenitors ($10\text{--}60 M_{\odot}$) to the number of AGB progenitors ($1.3\text{--}3.5 M_{\odot}$) varies from 0.1 for a Salpeter IMF (power-law slope $\alpha = -2.35$) up to 0.5 for an IMF with a slope $\alpha = -1.5$. The implication is that the sub-galactic fragments from which the outer halo was assembled formed stars with a flatter IMF, richer in massive stars leading to favored production of CEMP-no stars, while the inner halo was formed from fragments with relatively larger numbers of intermediate-mass stars, leading to greater production of CEMP-*s* stars.

Simulations of hierarchical galaxy formation suggest that the stars in the inner halo of the Milky Way formed preferentially from more massive sub-galactic fragments, capable of supporting extended star-formation histories (e.g., Zolotov et al. 2009; Font et al. 2011; McCarthy et al. 2012; Tissera et al. 2013a,b). By contrast, the outer halo is predominantly composed of stars formed in lower-mass fragments that were accreted over long periods of time, experienced short or truncated star-formation histories, and built up the outer halo as the sum of many disrupted former satellites. Thus, a possible link exists connecting higher-mass sub-galactic fragments, steeper IMFs, and the higher frequency of CEMP-*s* stars on the one hand, with lower-mass satellites, flatter IMFs, and a higher frequency of CEMP-no stars on the other.

While these connections are still somewhat speculative, there is now tentative evidence that lower-mass galaxies may form stars with flatter IMFs, at least over the limited mass ranges for which star-count IMFs can be obtained in photometric surveys. In particular, recent HST studies of the IMF in the Small Magellanic Cloud (Kalirai et al. 2013) and in two Ultra-faint Dwarf (UFD) satellites of the Milky Way (Brown et al. 2012), indicate a possible flattening trend in the IMF below $\sim 1 M_{\odot}$ with declining circular velocity (Geha et al. 2013). This trend continues for galaxies larger than the Milky Way, which appear to have formed stars with IMFs steeper than the Salpeter slope (Conroy et al. 2012). In addition, the limited available high-resolution spectroscopy for individual stars in UFDs indicates that the majority of the CEMP stars in these very low-mass galaxies are likely to be of the CEMP-no sub-class (Frebel & Norris 2013, Koch et al. 2013, and reference therein).

This line of reasoning sketches a possible scenario for explaining the variation of the relative numbers of CEMP-no and CEMP-*s* associated with the inner and outer halo. There are several steps in this logic that are unproven, thus the scenario must still be considered speculative. For example, the origins of CEMP-no stars may not be exclusively associated with massive progenitors. The flatter IMFs observed in the SMC and the UFDs may not continue with that slope into the range of intermediate and massive stars. Furthermore, the apparent trend of IMF slope with galaxy mass (Geha et al. 2013) may not be strictly valid, or it may instead be a trend with metallicity or some other environmental variable. Finally, the frequencies of CEMP stars need to be reproduced in the context of a detailed model that accounts simultaneously for the realistic merger histories of the halo components and the nucleosynthetic origins of their stars.

DC is an Australian Research Council Super Science Fellow. TCB acknowledges partial support from grant PHY 08-22648: Physics Frontier Center / Joint Institute for Nuclear Astrophysics (JINA), awarded by the U.S. National Science

Foundation. VMP acknowledges support from the Gemini Observatory. We thank an anonymous referee for comments that improved the presentation in this paper.

This research has made use of the SIMBAD and VIZIER services, operated at CDS, Strasbourg, France.

REFERENCES

- An, D., Beers, T. C., Johnson, J. A., et al. 2013, *ApJ*, 763, 65
- Aoki, W., Beers, T. C., Christlieb, N., et al. 2007, *ApJ*, 655, 492
- Aoki, W., Beers, T. C., Lee, Y. S., et al. 2013, *AJ*, 145, 13
- Beers, T. C., Preston, G. W., & Shectman, S. A. 1985, *AJ*, 90, 2089
- Beers, T. C., Preston, G. W., & Shectman, S. A. 1992, *AJ*, 103, 1987
- Beers, T. C., Chiba, M., Yoshii, Y., et al. 2000, *AJ*, 119, 2866
- Beers, T. C. & Christlieb, N. 2005, *ARA&A*, 43, 531
- Beers, T. C., Carollo, D., Ivezić, Z., et al. 2012, *ApJ*, 746, 34
- Bernstein, R., Shectman, S. A., Gunnels, S. M., Mochmacki, S., & Athey, A. E. 2003, *Proc. SPIE*, 4841, 1694
- Bisterzo, S., Gallino, R., Straniero, O., Cristallo, S., & Kappeler, F. 2011, *MNRAS*, 418, 284
- Bisterzo, S., Gallino, R., Straniero, O., Cristallo, S., & Kappeler, F. 2012, *MNRAS*, 422, 849
- Bovy, J., Hennawi, J. F., Hogg, D. W., et al. 2011, *ApJ*, 729, 141
- Bovy, J., Allende Prieto, C., Beers, T. C., et al. 2012, *ApJ*, 759, 131
- Brown, T. M., Tumlinson, J., Geha, M., et al. 2012, *ApJ*, 753, L21
- Caffau, E., Bonifacio, P., François, P., et al. 2011, *Nature*, 477, 67
- Carollo, D., Beers, T. C., Lee, Y. S., et al. 2007, *Nature*, 450, 1020 (C07)
- Carollo, D., Beers, T. C., Chiba, M., et al. 2010, *ApJ*, 712, 692 (C10)
- Carollo, D., Beers, T. C., Bovy, J., et al. 2012, *ApJ*, 744, 195
- Chiappini, C. 2013, *Astronomische Nachrichten*, 334, 595
- Chiba, M., & Beers, T. C. 2000, *AJ*, 119, 2843
- Christlieb, N., Green, P. J., Wisotzki, L., & Reimers, D. 2001, *A&A*, 375, 366
- Christlieb, N., Bessell, M. S., Beers, T. C., et al. 2002, *Nature* 419, 904
- Christlieb, N. 2003, *Reviews of Modern Astronomy*, 16, 191
- Christlieb, N., Schörck, T., Frebel, A., et al. 2008, *A&A*, 484, 721
- Cohen, J. G., Shectman, S. A., Thompson, I., et al. 2005, *ApJ*, 633, L109
- Cohen, J. G., Christlieb, N., Thompson, I., et al. 2013, *ApJ*, 778, 56
- Conroy, C. 2012, *ApJ*, 758, 21
- Dekker, H., D'Odorico, S., Kaufer, A., Delabre, B., & Kotzłowski, H. 2000, *Proc. SPIE*, 4008, 534
- de Jong, J. T. A., Yanny, B., Rix, H. W., Dolphin, A. E., Martin, N. F., & Beers, T. C. 2010, *ApJ*, 714, 663
- Font, A. S., McCarthy, I. G., Crain, R. A., et al. 2011, *MNRAS*, 416, 2802
- Frebel, A., Aoki, W., Christlieb, N., et al. 2005, *Nature*, 434, 871
- Frebel, A., Christlieb, N., Norris, J. E., et al. 2006, *ApJ*, 652, 1585
- Frebel, A. & Norris, J. E. 2013, in *Planets, Stars and Stellar System*, Vol. 5, eds T.D. Oswalt and G. Gilmore, Springer Science+Business Media (Dordrecht), p. 55
- Geha, M., Brown, T. M., Tumlinson, J., et al. 2013, *ApJ*, 771, 29
- Ghez, A. M., Salim, S., Weinberg, N. N., et al. 2008, *ApJ*, 689, 1044
- Gilbert, K., Beaton, R., Bullock, J., et al. 2013, *BAAS*, 221, 146.16
- Girard, T. M., van Altena, W. F., Zacharias, N., et al. 2011, *AJ*, 142, 15
- Grillmair, C. J. 2009, *ApJ*, 693, 1118
- Gunn, J. E., Siegmund, W. A., Mannery, E. J., et al. 2006, *AJ*, 131, 2332
- Hansen, T., Andersen, J., Nordström, B., Buchave, L. A., & Beers, T. C. 2011, *ApJ*, 743, L1
- Hansen, B. M. S., Kalirai, J. S., Anderson, J., et al. 2013a, *Nature*, 500, 51
- Hansen, T., Andersen, J., & Nordström, B. 2013b, *Proceedings of the XII International Symposium on Nuclei in the Cosmos (NIC XII)*, *Proceedings of Science* 146, 193
- Hattori, K., Yoshii, Y., Beers, T. C., Carollo, D., & Lee, Y. S. 2013, *ApJ*, 763, L17
- Herwig, F. 2005, *ARA&A*, 43, 435
- Hirschi, R., Fröhlich, C., Liebendörfer, M., & Thielemann, F.-K. 2006, *Reviews of Modern Astronomy*, 19, 101
- Ibata, R. A., Lewis, G. F., McConnachie, A. W., et al. 2013, *ApJ*, in press (arXiv:1311.5888)
- Ito, H., Aoki, W., Honda, S., & Beers, T. C. 2009, *ApJ*, 698, 37
- Ito, H., Aoki, W., Beers, T. C., Tominaga, N., Honda, S., & Carollo, D. 2013, *ApJ*, 773, 33
- Kafle, P. R., Sharma, S., Lewis, G. F., & Bland-Hawthorn, J. 2013, *MNRAS*, 430, 2973
- Kalirai, J. S. 2012, *Nature*, 486, 90
- Kalirai, J. S., et al. 2013, *ApJ*, 763, 110
- Keller, S. C., Bessel, M. S., Frebel, A., et al., 2014, *Nature*, (doi:10.1038/nature12990)
- Kinman, T. D., Cacciari, C., Bragaglia, A., Smart, R., & Spagna, A. 2012, *MNRAS*, 422, 2116
- Kobayashi, C., Tominaga, N., & Nomoto, K. 2011, *ApJ*, 730, L14
- Koch, A., Feltzing, S., Aden, D., & Matteucci, F. 2013, *A&A*, 554A, 5
- Koposov, S. E., Rix, H. W., & Hogg, D. W. 2009, *ApJ*, 712, 260
- Lee, Y. S., Beers, T. C., Masseron, T., et al. 2013, *AJ*, 146, 132
- Lucatello, S., Gratton, R. G., Beers, T. C., & Carretta, E. 2005, *ApJ*, 625, 833
- Lucatello, S., Beers, T. C., Christlieb, N. C., et al. 2006, *ApJ*, 652, L37
- Lugaro, M., Karakas, A. I., Stancliffe, R. J., & Rijs, C. 2012, *ApJ*, 747, 2
- Marsteller, B., Beers, T. C., Rossi, S., Christlieb, N., Bessell, M., & Rhee, J. 2005, *Nucl. Phys. A.*, 758, 312
- McCarthy, I. G., Font, A. S., Crain, R. A., Deason, A. J., Schaye, J., & Theuns, T. 2012, *MNRAS*, 420, 2245
- Meynet, G., Ekström, S., & Maeder, A. 2006, *A&A*, 447, 623
- Meynet, G., Hirschi, R., Ekström, S., et al. 2010, *A&A*, 521, A30
- Munn, J. A., Monet, D. G., Levine, S. E., et al. 2004, *AJ*, 127, 3034
- Munn, J. A., Monet, D. G., Levine, S. E., et al. 2008, *AJ*, 136, 895
- Noguchi, K., Aoki, W., Kawanomoto, S., et al. 2002, *PASJ*, 54, 855
- Nomoto, K., Kobayashi, C., & Tominaga, N. 2013, *ARA&A*, 51, 457
- Norris, J. E., Ryan, S. G., & Beers, T. C. 1997, *ApJ*, 488, 350
- Norris, J. E., Christlieb, N., Korn, A. J., et al. 2007, *ApJ*, 670, 774
- Norris, J. E., Bessell, M. S., Yong, D., et al. 2013a, *ApJ*, 762, 25
- Norris, J. E., Bessell, M. S., Yong, D., et al. 2013b, *ApJ*, 762, 28
- Placco, V. M., Frebel, A., Beers, T. C., et al. 2013, *ApJ*, 770, 104
- Roederer, I. U., Preston, G. W., Thompson, I. B., Shectman, S. A., Kelson, D., & Sneden, C. 2014, *AJ*, submitted
- Roeser, S., Demleitner, M., & Schilbach, E., 2010, *AJ*, 139, 2440
- Rossi, S., Beers, T. C., & Sneden, C. 1999, in *The Third Stromlo Symposium, ASP Conference Series*, eds B. K. Gibson, T. S. Axelrod, and M. E. Putman, 165, p. 264
- Rossi, S., Beers, T. C., Sneden, C., Sevastyanenko, T., Rhee, J., & Marsteller, B. 2005, *AJ*, 130, 2804
- Sarajedini, A., Yang, S. C., Monachesi, A., Lauer, T. R., & Trager, S. C. 2012, *MNRAS*, 425, 1459
- , Schönrich, R., Asplund, M., & Casagrande, L. 2011, *MNRAS*, 415, 3807
- Sneden, C., Cowan, J. J., & Gallino, R. 2008, *ARA&A*, 46, 241
- Spite, M., Caffau, E., Bonifacio, P., et al. 2013, *A&A*, 552, 107
- Suda, T., Fujimoto, M. Y., & Itoh, N. 2007, *ApJ*, 667, 1206
- Tissera, P. B., Scannapieco, C., Beers, T. C., & Carollo, D. 2013, *MNRAS*, 432, 3391
- Tissera, P. B., Beers, T. C., Carollo, D., & Scannapieco, C. 2013, *MNRAS*, in press (arXiv:1309:3609)
- Tominaga, N., Umenda, H., & Nomoto, K. 2007, *ApJ*, 660, 516
- Tominaga, N., Iwamoto, N., & Nomoto, K. 2013, *ApJ*, in press (arXiv:1309.6734)
- Tumlinson, J. 2007a, *ApJ*, 664, L63
- Tumlinson, J. 2007b, *ApJ*, 665, 1361
- Umeda, H., & Nomoto, K. 2003, *Nature*, 422, 871
- Umeda, H., & Nomoto, K. 2005, *ApJ*, 619, 427
- Vogt, S. S., Allen, S. L., Bigelow, B. C. et al. 1994, *Proc. SPIE*, 2198, 362
- Wisotzki, L., Koehler, T., Groote, D., & Reimers, D. 1996, *A&AS*, 115, 227
- Yanny, B., Rockosi, C. M., Newberg, H. J., et al. 2009, *AJ*, 137, 4377
- Yong, D., Norris, J. E., Bessell, M. S., et al. 2013, *ApJ*, 762, 26
- York, D. G., Adelman, J., Anderson, J. E., et al. 2000, *AJ*, 120, 1579
- Zacharias, N., Finch, C. T., Girard, T. M., et al. 2013, *AJ*, 145, 44
- Zolotov, A., et al. 2009, *ApJ*, 702, 1058

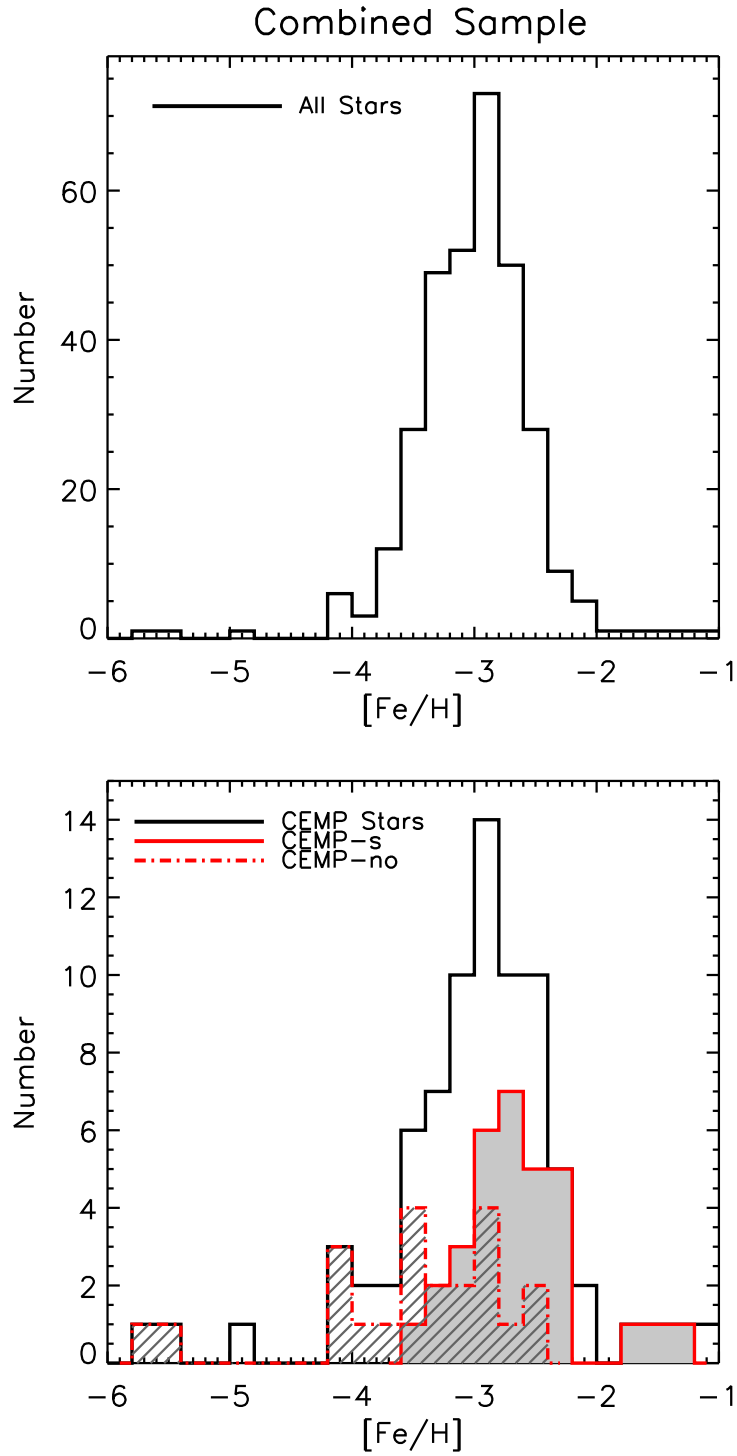


FIG. 1.— Top panel: The metallicity distribution function (MDF) for the combined sample of stars from Aoki et al. (2013) & Yong et al. (2013), 323 stars. Bottom panel: MDFs for the sub-sample of CEMP stars (SS, ES, CSS, or CES; black unshaded histogram, 96 stars), CEMP-s (SS or ES; gray histogram, red line, 42 stars) and CEMP-no (SS or ES; cross-hatched histogram, dashed red line, 46 stars).

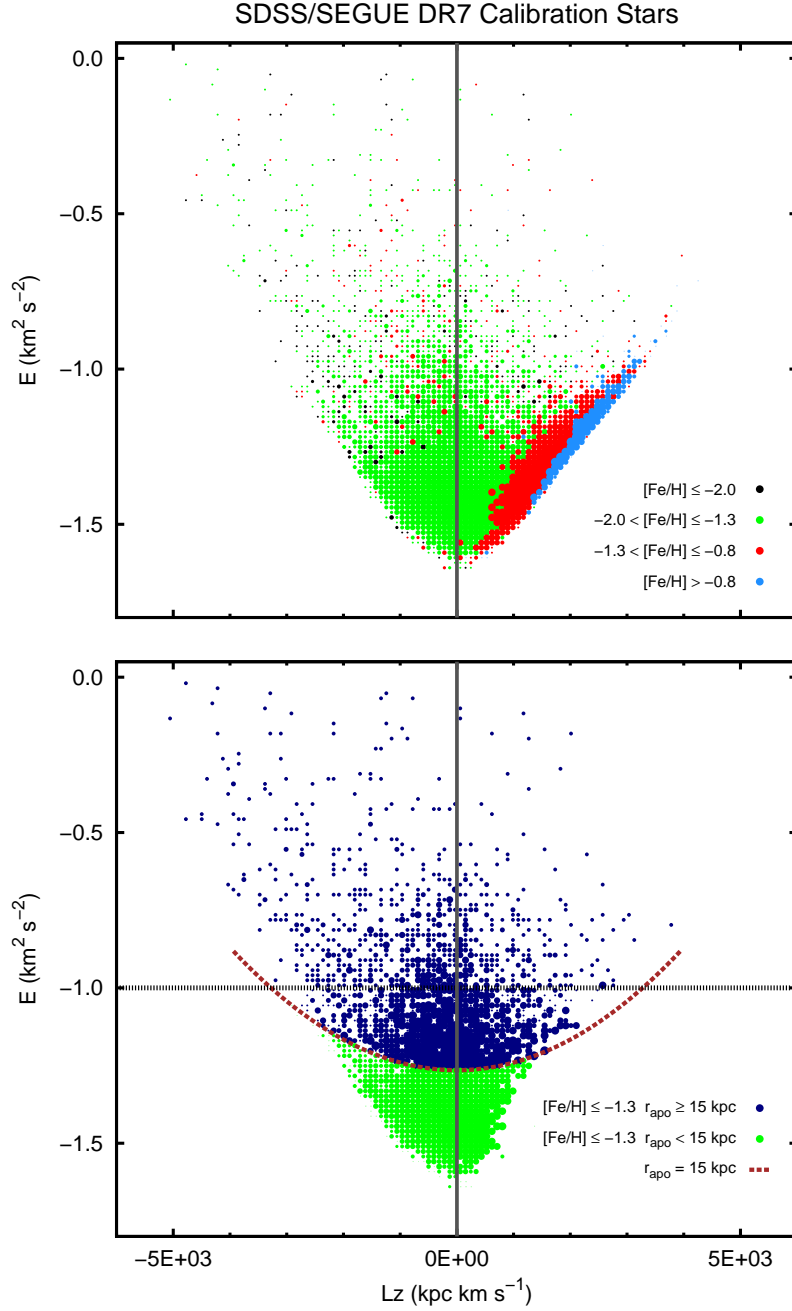


FIG. 2.— Top panel: Lindblad diagram for the sample of 23351 SDSS/SEGUE DR7 calibration stars from C10 (energy is in units of 10^5). The colors represent different ranges of metallicity, corresponding to the thick disk (light blue dots), metal-weak thick disk (red dots), inner halo (green dots), and outer halo (black dots). The point size is proportional to the logarithmic number density at a given point of the diagram. The vertical line divides this diagram at $L_Z = 0$; prograde stars have $L_Z > 0$, while retrograde stars have $L_Z < 0$. Bottom panel: Lindblad diagram for the 10431 SDSS/SEGUE DR7 calibration stars with metallicities $[\text{Fe}/\text{H}] \leq -1.3$. The green dots represent the 7809 stars with apo-Galactic distances $r_{\text{apo}} \leq 15$ kpc, while the blue dots denote the 2622 stars in the same range of metallicity but with apo-Galactic distance $r_{\text{apo}} > 15$ kpc. The red dashed curve represents the locus of the points with constant apo-Galactic radii, $r_{\text{apo}} = 15$ kpc, while the horizontal line at $E = -1.0$ shows (roughly) the energy of the transition zone between the inner- and outer-halo components (see text). The vertical line divides this diagram at $L_Z = 0$; prograde stars have $L_Z > 0$, while retrograde stars have $L_Z < 0$. Note the preponderance of retrograde motions among the likely outer-halo stars located above the $E = -1.0$ line.

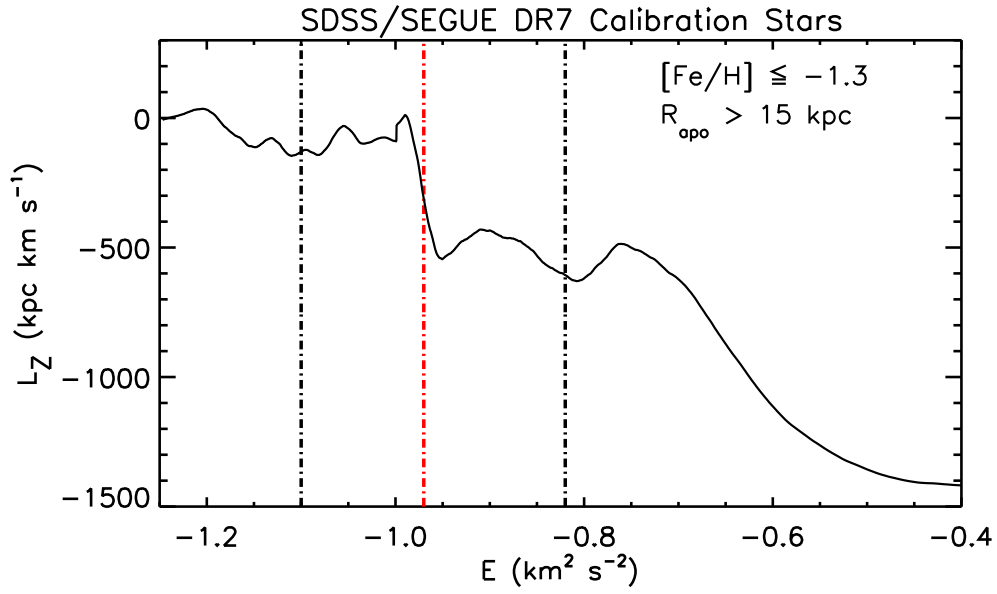


FIG. 3.— Mean angular momentum in the z direction as a function of the total energy (in units of 10^5) for the 8039 SDSS/SEGUE DR7 calibration stars with metallicity $[\text{Fe}/\text{H}] \leq -1.3$ and $r_{\text{apo}} > 15$ kpc. A moving average with overlapping bins of 200 stars is applied. The vertical red dot-dashed line denotes the mean point of the transition zone between the inner halo and outer halo, while the vertical black dot-dashed lines represents the adopted transition zone.

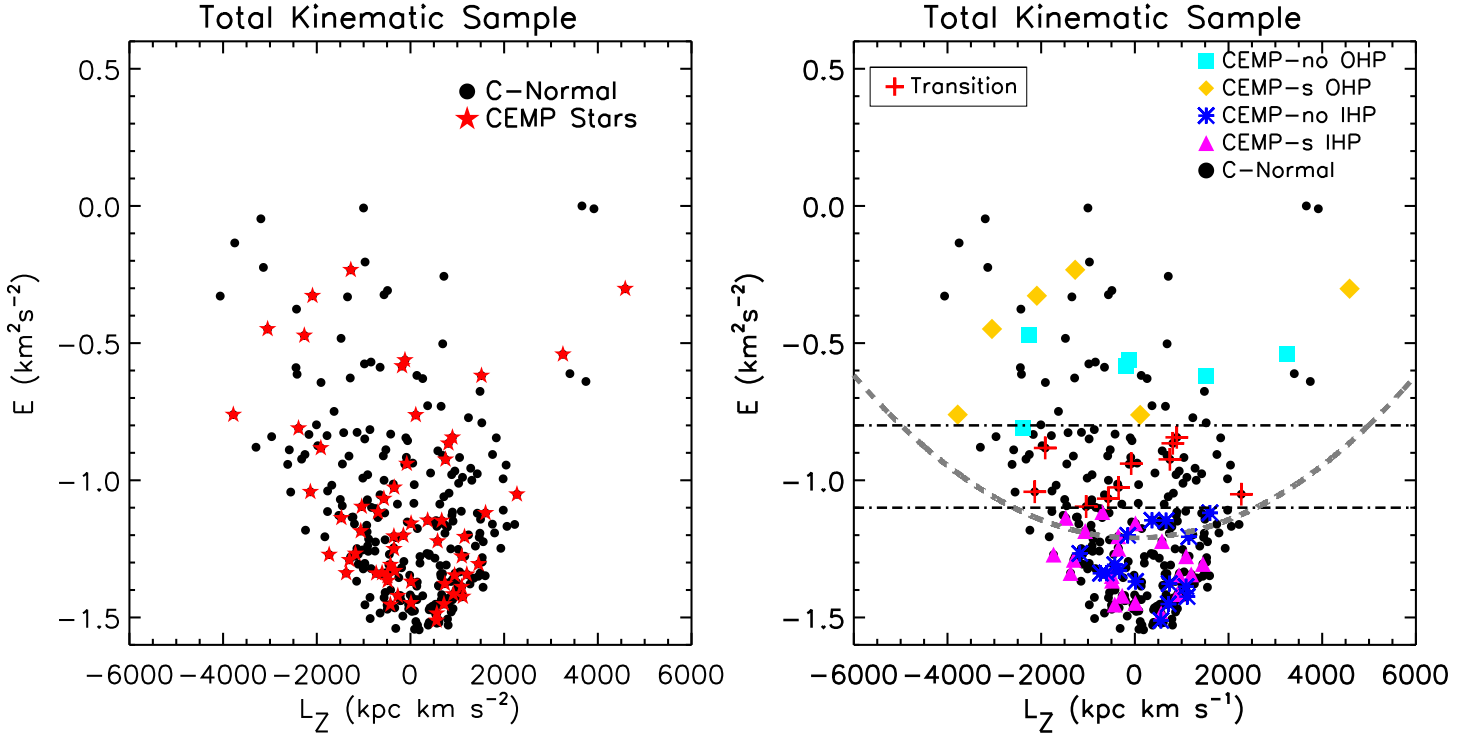


FIG. 4.— Total energy vs. angular momentum in the z direction for the 301 stars in the Total Kinematic Sample. Left panel: C-normal stars are represented by black dots, while CEMP stars (ES and CES) are denoted by red stars. Right panel: The same sample of stars, with purple filled triangles and blue asterisks indicating CEMP- s and CEMP-no members of the inner halo (ES only), respectively. Yellow filled diamonds and light blue filled squares represent CEMP- s and CEMP-no members of the outer halo (ES only), respectively. The red crosses are CEMP- s and CEMP-no stars located in the transition zone between the inner halo and the outer halo, with similar probability to be members of these components (ES only). C-normal (or indeterminate) stars are indicated with black dots. The light gray dashed curve denotes the locus of the points that possess constant apo-Galactic radius, $r_{\text{apo}} = 15$ kpc, while the dark gray dot-dashed horizontal lines shows the values of the energies delimiting the transition zone.

TABLE 1
PARAMETERS FOR THE SAMPLE OF AOKI ET AL. (2013)

Name	T_{eff} (K)	log(g)	[Fe/H]	V_{rad} (km s ⁻¹)	$\sigma_{V_{\text{rad}}}$ (km s ⁻¹)	RA (deg)	DEC (deg)	PM_{RA} (mas yr ⁻¹)	PM_{DEC} (mas yr ⁻¹)	$\sigma_{PM_{\text{RA}}}$ (mas yr ⁻¹)	$\sigma_{PM_{\text{DEC}}}$ (mas yr ⁻¹)	d (kpc)	[C/Fe]	[Ba/Fe]	C	Ba	CEMP Class	Sample	Member
(1)	(2)	(3)	(4)	(5)	(6)	(7)	(8)	(9)	(10)	(11)	(12)	(13)	(14)	(15)	(16)	(17)	(18)	(19)	(20)
2174-53521-423	6450	4.0	-3.39	-51.1	0.3	250.022	37.152	-5.72	5.64	2.72	2.72	2.10	0	0			I
1690-53475-323 ^c	6100	4.0	-3.05	-18.7	0.2	251.542	28.406	-16.01	45.77	2.59	2.59	2.07	+2.52	+1.78	3	3	s	1100	U
2180-54613-258	6600	4.0	-2.56	-33.1	0.3	252.569	22.704	-5.93	-8.72	2.68	2.68	2.68	0	0			I
0974-52427-332	6050	4.0	-3.24	-42.5	0.1	254.895	35.265	-17.92	-37.19	2.73	2.73	3.18	0	0			O
2808-54524-510	5100	4.8	-3.21	-174.9	0.2	255.915	28.614	-27.48	-129.90	2.46	2.46	0.57	+0.28	...	2	0			I
2797-54616-258	6350	4.0	-2.85	-353.4	0.2	262.195	6.951	2.04	-19.18	2.28	2.28	2.81	0	0			I
2799-54368-138	5200	2.7	-2.51	-211.9	0.1	263.575	43.268	0.79	-5.95	2.45	2.45	15.86	+1.78	+1.61	3	3	s	1100	O
2799-54368-502	5250	2.0	-3.29	-142.3	0.1	263.884	44.777	-6.71	0.94	2.43	2.43	12.00	0	0			T
2799-54368-560	5450	3.0	-2.93	-310.1	0.1	264.117	44.343	-1.30	-5.39	2.43	2.43	10.55	...	-0.47	0	4			T
2183-53536-175 ^c	5350	2.6	-3.17	78.7	0.2	266.601	24.930	-6.70	0.91	2.39	2.39	11.26	+1.24	+0.26	3	2	no	0100	O
2798-54397-354	6550	4.0	-3.01	-271.0	0.2	277.691	41.691	-0.56	21.55	2.54	2.54	2.65	0	0			T
2534-53917-002	6550	4.0	-1.98	-17.5	0.2	278.560	20.393	-13.36	0.61	2.54	2.54	3.10	0	0			I
2552-54632-090	5350	3.0	-2.85	-423.3	0.2	279.007	63.291	-5.03	-1.39	2.36	2.36	0.79	+2.02	+2.37	3	3	s	1100	I
2303-54629-377	6600	4.0	-3.34	-55.6	0.3	301.306	-10.751	17.34	-2.94	2.32	2.32	3.10	0	0			I
2815-54414-098	6050	4.0	-2.80	-184.2	0.1	313.220	1.161	-7.81	-3.23	2.63	2.63	3.41	0	0			I
1918-53240-306	5250	2.0	-3.43	-110.6	0.2	316.228	-1.078	0.21	2.72	2.58	2.58	11.70	...	-0.72	0	4			T
1112-53180-325	6250	4.0	-2.75	-270.6	0.2	317.856	1.156	5.79	-13.80	2.26	2.26	3.02	...	+0.07	0	2			I
2305-54414-429	6650	4.0	-2.91	-199.7	0.8	319.709	-6.682	8.97	-4.38	2.73	2.73	3.01	0	0			I
2305-54414-081	6350	4.0	-2.88	-167.3	0.2	320.795	-8.344	-0.66	-35.54	2.73	2.73	3.11	0	0			T
0641-52199-315	6150	4.0	-2.76	-178.2	0.1	322.172	-7.941	-5.78	-3.11	2.70	2.70	3.02	...	+0.58	0	3			I
2309-54441-290 ^c	5100	2.1	-3.17	14.9	0.1	331.693	-9.429	1.86	2.68	2.68	2.68	9.81	+0.64	-0.85	2	4	no	0100	I
2251-53557-279	6200	4.0	-2.42	-150.8	0.2	331.931	20.298	10.44	10.96	2.40	2.40	3.65	...	-0.42	0	4			T
2308-54379-227	6450	4.0	-2.85	-136.5	0.2	332.190	6.228	-1.52	-11.00	2.45	2.45	2.01	0	0			I
2309-54441-564	5150	1.8	-2.55	-392.4	0.1	333.392	-7.434	-1.26	-1.97	2.60	2.60	13.49	...	-0.69	0	4			T
2310-53710-131	6450	4.0	-2.94	-244.7	0.2	345.110	5.999	6.40	-10.22	2.44	2.44	2.92	0	0			I
0726-52226-335	6100	4.0	-2.74	-111.4	0.2	347.062	-8.924	25.45	5.67	2.66	2.66	2.66	0	0			T
2623-54096-458	6350	4.0	-3.09	-307.5	0.6	347.498	23.134	3.20	-8.64	2.50	2.50	2.22	0	0			I
0747-52234-337	6550	4.0	-2.91	-130.1	0.3	353.513	15.641	37.81	-14.62	2.56	2.56	2.56	0	0			T
2622-54095-483	4900	1.9	-3.12	-156.9	0.2	354.573	9.035	-0.61	-1.39	2.35	2.35	17.13	...	-0.75	0	4			T
1882-53262-132	6250	4.0	-3.20	-87.4	1.1	357.415	38.538	35.39	12.12	2.51	2.51	3.02	0	0			O
1489-52991-251 ^c	5200	4.8	-3.20	-9.4	0.2	359.329	-0.880	46.27	-171.80	2.55	2.55	0.64	+0.57	+1.33	2	3	s	0100	T

TABLE 1
PARAMETERS FOR THE SAMPLE OF AOKI ET AL. (2013)

Name	T_{eff} (K)	$\log(g)$	[Fe/H]	V_{rad} (km s ⁻¹)	$\sigma_{V_{\text{rad}}}$ (km s ⁻¹)	RA (deg)	DEC (deg)	PM_{RA} (mas yr ⁻¹)	PM_{DEC} (mas yr ⁻¹)	$\sigma_{PM_{RA}}$ (mas yr ⁻¹)	$\sigma_{PM_{DEC}}$ (mas yr ⁻¹)	d (kpc)	[C/Fe]	[Ba/Fe]	C	Ba	CEMP Class (18)	Sample (19)	Member (20)
(1)	(2)	(3)	(4)	(5)	(6)	(7)	(8)	(9)	(10)	(11)	(12)	(13)	(14)	(15)	(16)	(17)	(18)	(19)	(20)

NOTE. — In column (16) the identifier “C” is a flag indicating the following:

C = 0: No carbon is detected (carbon-unknown).

C = 1: Carbon measurement indicates upper limit on [C/Fe] > +0.7 (carbon-indeterminate).

C = 2: Carbon measurement indicates [C/Fe] < +0.7 or upper limit on [C/Fe] indicates [C/Fe] < +0.7 (carbon-normal).

C = 3: Carbon measurement indicates [C/Fe] ≥ +0.7 or lower limit on [C/Fe] indicates [C/Fe] > +0.7 (carbon-enhanced).

In column (17) the identifier “Ba” is a flag indicating the following:

Ba = 0: No barium is detected (barium-unknown).

Ba = 1: Barium measurement indicates upper limit on [Ba/Fe] > 0.0 (barium-indeterminate).

Ba = 2: Barium measurement indicates 0.0 < [Ba/Fe] < +1.0 (barium-normal).

Ba = 3: Barium measurement indicates [Ba/Fe] ≥ +1.0 (barium-enhanced).

Ba = 4: Barium measurement indicates x[Ba/Fe] ≤ 0.0 or upper limit on [Ba/Fe] ≤ 0 (barium-deficient).

Column (18) indicates the adopted CEMP-subclass (CEMP-s or CEMP-no); column (19) indicates the assignment into the sub-sample used for the kinematic analysis in the form of a 4 digit code, with each digit set to 1 if the star is a member of the sub-sample, 0 if not, in the order – Strict Sample (SS), Extended Sample (ES), CEMP star without sub-class assignment in Strict Sample (CSS), and CEMP star without sub-class assignment in Extended Sample (CES); column (20) indicates the halo component into which stars with kinematic information have been assigned based on the criteria described in the text. “O” indicates outer halo, “I” indicates inner halo, “T” indicates the transition zone, and “U” indicates that the star was unclassified (star is on an unbound orbit, or is missing the information required for making this assignment).

^a This star does not have a well-measured distance available.

^b This star does not have a well-measured proper motion available.

^c This star is unbound from the Galaxy, according to its derived orbital parameters.

^d Unknown [Ba/Fe], but classified as CEMP-no by Aoki et al. (2013).

^e Likely CEMP (+0.5 ≤ [C/Fe] < +0.7); CEMP-s (Ba ≥ +0.8); CEMP-no (0.0 ≤ [Ba/Fe] ≤ +0.3, or based on pattern of light-element abundances).

^f This star is also in the Yong et al. sample – 2848-54453-252 = CS 29527-015; 2044-53327-515 = 53327-2044-515; 2667-54142-094 = 54142-2667-094; 2036-53446-324 = 53436-1996-093

TABLE 2
PARAMETERS FOR THE SAMPLE OF YONG ET AL. (2013)

Name	T_{eff}	$\log(g)$	[Fe/H]	V_{rad}	$\sigma_{V_{\text{rad}}}$	RA	DEC	PM_{RA}	PM_{DEC}	$\sigma_{PM_{\text{RA}}}$	$\sigma_{PM_{\text{DEC}}}$	d	[C/Fe]	[Ba/Fe]	C	Ba	CEMP	Sample	Member
(1)	(K)	(3)	(4)	(km s ⁻¹)	(km s ⁻¹)	(deg)	(deg)	(mas yr ⁻¹)	(mas yr ⁻¹)	(mas yr ⁻¹)	(mas yr ⁻¹)	(kpc)	(14)	(15)	(16)	(17)	Class	(19)	(20)
CS 22948-066 ⁱ	5077	2.2	-3.20	-170.6	1.0	326.213	-37.465	-2.0	-5.5	1.2	1.2	4.42	-0.74	-1.15	2	4			I
HE 2142-5656	4939	1.9	-2.87	103.4	0.5	326.585	-56.705	-7.0	-5.2	0.7	0.8	6.86	+0.95	-0.63	3	4	no	1100	I
CS 22944-032	5293	2.8	-2.98	17.1	0.2	326.930	-13.673	-10.2	-47.0	1.8	1.9	2.09	+0.31	-0.76	2	4			T
CS 22948-093	6609	4.2	-3.17	364.3	0.3	327.631	-41.130	-18.4	-20.3	2.1	1.9	1.69	0	0			O
CS 22956-050	4844	1.6	-3.39	-0.1	1.0	329.524	-65.224	-2.4	-3.1	2.1	2.2	11.91	+0.27	-0.78	2	4			I
HE 2158-0348 ^c	5150	2.4	-2.57	67.6	1.5	330.167	-3.570	12.4	-11.1	3.8	3.8	8.83	+1.87	+1.75	3	3	s	1100	U
BS 17569-049	4645	1.1	-2.84	-213.1	1.0	331.243	4.026	0.6	-4.4	3.8	3.8	11.61	-0.12	+0.20	2	2			I
HE 2202-4831	5331	3.0	-2.78	56.2	0.5	331.524	-48.281	-5.7	-8.5	1.8	2.0	5.60	+2.41	-1.28	3	4	no	1100	I
CS 22965-054 ^d	6137	3.7	-3.10	-282.3	0.3	331.626	-2.543	26.0	0.0	1.0	3.0	2.30	+0.62	< -0.48	2	4	no	0100	T
HE 2209-1240	6319	3.8	-2.59	22.1	1.5	332.953	-12.429	13.0	-14.4	4.5	2.4	3.06	...	-0.13	0	4			I
CS 22892-052	4825	1.5	-3.03	13.0	0.8	334.257	-16.658	8.9	-4.2	1.8	3.8	7.33	+1.05	+0.96	3	2		0011	T
CS 22886-042	4798	1.5	-2.83	-221.4	0.1	335.108	-10.389	5.0	-6.4	4.0	4.0	7.80	+0.12	-0.32	2	4			I
CS 29502-042	5039	2.1	-3.27	-138.1	1.0	335.453	2.479	-1.8	-7.7	3.7	3.7	3.47	+0.16	-1.69	2	4			I
CS 29502-092	5074	2.2	-2.99	-68.7	0.2	335.650	-1.641	11.7	-72.4	1.7	1.7	1.85	+0.96	-1.20	3	4	no	1100	O
HE 2221-0453 ^c	4430	0.7	-2.00	-189.9	0.1	336.107	-4.634	2.2	-9.6	2.9	2.9	15.71	+1.83	+1.76	3	3	s	1100	U
CS 29516-024 ^c	4637	1.0	-3.05	-84.3	1.0	336.564	2.863	-1.6	-39.7	3.7	3.7	13.04	-0.06	-0.90	2	4			U
HE 2228-0706	5003	2.0	-2.78	-11.7	0.1	337.852	-6.848	-5.3	-14.2	1.6	1.6	4.61	+2.32	+2.46	3	3	s	1100	I
HE 2232-0603	6085	3.8	-1.46	-61.2	1.5	338.698	-5.805	2.4	-20.7	4.4	4.4	3.62	+1.22	+1.50	3	3	s	1100	I
CS 29491-053	4700	1.2	-3.03	-147.5	1.0	339.235	-28.518	1.8	-9.9	1.4	1.5	8.85	-0.27	-0.89	2	4			I
HE 2246-2410	6431	4.4	-2.96	-3.1	1.8	342.249	-23.911	2.0	-28.0	1.0	3.0	1.48	< +1.39	< -0.30	1	4			I
HE 2247-7400	4829	1.6	-2.87	5.7	0.5	342.831	-73.740	-2.6	-0.4	1.4	1.4	7.88	+0.70	-0.94	3	4	no	1100	I
CD-24:17504 ^c	6236	3.7	-3.38	135.9	1.0	346.834	-23.877	202.0	-185.8	2.3	1.6	0.70	...	< -0.59	0	4			U
CS 22888-031	6241	4.5	-3.31	-125.1	0.3	347.885	-35.445	58.0	-27.7	1.6	1.6	0.94	+0.38	...	2	0			I
CS 30338-089	4886	1.7	-2.78	-113.1	0.1	348.958	10.324	3.5	0.4	3.7	3.7	9.43	+2.06	+2.30	3	3	s	1100	I
HE 2323-0256 ^f	4958	1.8	-3.97	-125.8	1.3	351.624	-2.666	5.1	-3.3	3.8	3.8	7.50	+1.06	-0.52	3	4	no	1100	I
HE 2330-0555 ^c	4867	1.6	-2.98	-235.0	0.1	353.228	-5.647	5.5	-14.1	4.1	4.1	11.90	+2.09	+1.17	3	3	s	1100	U
CS 22966-011	6298	4.4	-3.02	-13.5	0.3	353.779	-30.382	34.1	-43.4	2.4	1.5	0.87	+0.45	-0.05	2	4			I
CS 22952-015	4824	1.5	-3.44	-19.2	0.8	354.370	-5.799	3.4	-10.7	4.0	4.0	7.89	-0.41	-1.33	2	4			I
HE 2341-2029 ^h	6507	4.3	-2.60	-83.0	1.5	356.082	-20.222	25.8	-16.9	3.6	3.5	2.41	+1.05	-0.42	3	4	no	1100	I
CS 29522-046	5974	3.7	-2.12	-106.8	0.2	356.249	8.781	85.1	-4.7	2.2	2.2	0.71	+0.42	-0.13	2	4			I
HE 2344-2800	6624	4.1	-2.65	-135.8	1.0	356.685	-27.736	-5.4	-33.0	1.6	1.7	1.70	...	-0.37	0	4			I
CS 22966-057	5364	3.1	-2.43	101.2	1.0	357.241	-29.656	4.5	-34.9	1.6	1.4	2.77	+0.06	-0.24	2	4			I
CS 29499-060	6595	4.1	-2.50	-58.7	0.3	358.418	-26.979	60.7	15.7	1.5	1.4	0.77	+0.38	...	2	0			I
HE 2356-0410 ^g	5170	2.5	-3.19	-61.5	1.5	359.805	-3.897	8.2	-22.6	3.9	3.9	3.53	+2.27	-0.80	3	4	no	1100	I

CEMP Sub-Classes in the Halo System

TABLE 2
PARAMETERS FOR THE SAMPLE OF YONG ET AL. (2013)

Name	T_{eff} (K)	log(g)	[Fe/H]	V_{rad} (km s ⁻¹)	$\sigma_{V_{\text{rad}}}$ (km s ⁻¹)	RA (deg)	DEC (deg)	PM_{RA} (mas yr ⁻¹)	PM_{DEC} (mas yr ⁻¹)	$\sigma_{PM_{RA}}$ (mas yr ⁻¹)	$\sigma_{PM_{DEC}}$ (mas yr ⁻¹)	d (kpc)	[C/Fe]	[Ba/Fe]	C	Ba	CEMP Class	Sample	Member
(1)	(2)	(3)	(4)	(5)	(6)	(7)	(8)	(9)	(10)	(11)	(12)	(13)	(14)	(15)	(16)	(17)	(18)	(19)	(20)

NOTE. — In column (16) the identifier “C” is a flag indicating the following:
C = 0: No carbon is detected (carbon-unknown).

C = 1: Carbon measurement indicates upper limit on [C/Fe] > +0.7 (carbon-indeterminate).
C = 2: Carbon measurement indicates [C/Fe] < +0.7 or upper limit on [C/Fe] indicates [C/Fe] < +0.7 (carbon-normal).
C = 3: Carbon measurement indicates [C/Fe] ≥ +0.7 or lower limit on [C/Fe] indicates [C/Fe] > +0.7 (carbon-enhanced).
In column (17) the identifier “Ba” is a flag indicating the following:

Ba = 0: No barium is detected (barium-unknown).

Ba = 1: Barium measurement indicates upper limit on [Ba/Fe] > 0.0 (barium-indeterminate).
Ba = 2: Barium measurement indicates 0.0 < [Ba/Fe] < +1.0 (barium-normal).
Ba = 3: Barium measurement indicates [Ba/Fe] ≥ +1.0 (barium-enhanced).
Ba = 4: Barium measurement indicates [Ba/Fe] ≤ 0.0 or upper limit on [Ba/Fe] ≤ 0 (barium-deficient).

Column (18) indicates the adopted CEMP-subclass (CEMP-*s* or CEMP-no); column (19) indicates the assignment into the sub-sample used for the kinematic analysis in the form of a 4 digit code, with each digit set to 1 if the star is a member of the sub-sample, 0 if not, in the order – Strict Sample (SS), Extended Sample (ES), CEMP star without sub-class assignment in Strict Sample (CSS), and CEMP star without sub-class assignment in Extended Sample (CES); column (20) indicates the halo component into which stars with kinematic information have been assigned based on the criteria described in the text. “O” indicates outer halo, “I” indicates inner halo, “T” indicates the transition zone, and “U” indicates that the star was unclassified (star is on an unbound orbit, or is missing the information required for making this assignment).

^a This star does not have a well-measured distance available.

^b This star does not have a well-measured proper motion available.

^c This star is unbound from the Galaxy, according to its derived orbital parameters.

^d Likely CEMP (0.5 ≤ [C/Fe] < +0.7); CEMP-*s* ([Ba/Fe] ≥ +0.8); CEMP-no (0.0 ≤ [Ba/Fe] ≤ +0.3, or based on pattern of light-element abundances).

^e Likely CEMP-no based on the luminosity criteria of Aoki et al. (2007) and the observed [Ba/Fe] ratio.

^f CS 22949-037

^g CS 22957-027

^h Elemental abundances taken from Cohen et al. (2013)

ⁱ Elemental abundances taken from Roederer et al. (2014)

^j This star is also in the Aoki et al. sample – CS 29527-015 = 2848-54453-252; 53327-2044-515 = 2044-53327-515; 54142-2667-094 = 2667-54142-094; 53436-1996-093 = 2036-53446-324

TABLE 3
KINEMATIC MEMBERSHIP SUMMARY

Member	Total	no	s
Total Kinematic Sample			
O	46
I	190
T	65
U	22
CEMP Kinematic Sample			
O	12 (20)	6 (14)	6 (6)
I	37 (48)	16 (27)	21 (21)
T	5 (10)	0 (3)	5 (7)
U	10 (10)	2 (2)	8 (8)

NOTE. — The column labeled “Member” indicates the halo component into which stars with kinematic information have been assigned, based on the criteria described in the text. “O” indicates outer halo, “I” indicates inner halo, “T” indicates the transition zone, and “U” indicates that the star was unclassified (unbound orbits). The upper section of the table pertains to the Total Kinematic Sample of program stars, including those without measurements of carbon available, or that are simply C-normal. The lower section pertains to the CEMP Kinematic Sample, including only stars that are considered C-enhanced. The first number in each column pertains to stars in the SS, the second number (in parentheses) in each column pertains to stars in the ES.